energy&fuels

pubs.acs.org/EF
Article

From Bulk to Surface: A First-Principles Study of Cu Doping in ZnO and Its Implications for Photocatalysis

Published as part of Energy & Fuels special issue "Novel Routes to Green Hydrogen Production in Europe".

Michele Loriso and Francesco Ambrosio*

Cite This: *Energy Fuels* 2026, 40, 3397−3407

Read Online

ACCESS | Metrics & More | Article Recommendations | Supporting Information

ABSTRACT: Cu-doped ZnO has long been discussed for its optoelectronic properties, and, more recently, renewed interest has been prompted by applications in heterogeneous photocatalysis. In this study, we investigate copper defects, namely, substitutional (Cu_{Zn}) and interstitial (Cu_i), in bulk ZnO and at its ($10\bar{1}0$) surface using advanced electronic-structure calculations. In the bulk, Cu_{Zn} and Cu_i are found to feature deep donor and acceptor states, respectively. This explains why achieving *p*-type conductivity through Cu doping is highly unlikely, while the characteristic green luminescence of Cu-doped ZnO is induced by donor-related transitions involving Cu_{Zn}. The physical picture appears remarkably different on the surface: by aligning the energy levels of Cu defects at the semiconductor−water interface, it is observed that surface Cu_{Zn}, possessing both donor and acceptor states suitably aligned with the redox potentials of aqueous species, can promote both the reduction and oxidation processes of the water-splitting reaction. Instead, surface Cu_i, while sizably stabilized at higher Cu concentrations, is predicted to have a less advantageous or even detrimental impact on the photocatalytic activity of ZnO. These results indicate that the relative population of substitutional and interstitial surface defects, tuned by the experimental conditions, is a key factor in determining the efficiency of Cu-doped ZnO for photocatalytic water splitting.

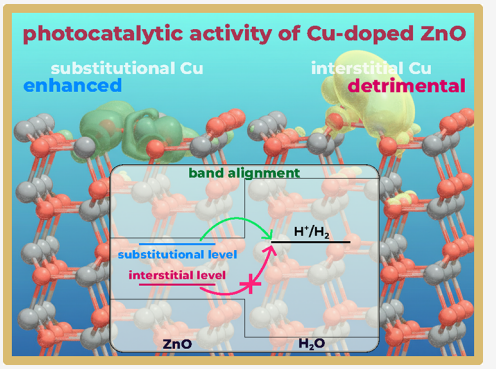

1. INTRODUCTION

Wurtzite zinc oxide, ZnO, is a transparent semiconductor that has been subject to extensive research,[1−3] in virtue of its optoelectronic properties, which, coupled with its earth-abundance and chemical stability, make it suitable for a variety of technological applications. These include light-emitting diodes,[4,5] solar cells (mainly as an electron transport layer or transparent electrode),[6−10] sensors for a wide variety of gas species,[11−13] piezoelectric devices,[14,15] phosphorescent thin films,[16] and photocatalysis.[17−20] ZnO possesses a fundamental band gap in the UV region (3.44 eV at 4 K,[21] 3.37 eV at room temperature[22]) and relatively high exciton binding energy (60 meV[1]). It shows a native tendency to be a *n*-type semiconductor, i.e. its Fermi level is usually pinned close to the conduction band edge as a consequence of intrinsic defects and impurities, which also make *p*-doping of the material extremely arduous.[23,24] For these reasons, appropriate doping of the material is often key to its effective inclusion in optoelectronic devices.[23,25−27]

Among the plethora of possible dopants,[1] Cu has been studied since the early 1960s[28,29] and has remained a topic of discussion ever since.[30−39] Interest for Cu inclusion in ZnO was initially fueled by attempts of *p*-doping this material.[1] Although a few reports claimed *p*-type conductivity of Cu-doped ZnO samples,[40] electronic-structure calculations and spectroscopic measurements seem to convene that incorporation of Cu in the ZnO lattice induces deep donor and/or acceptor states in the band gap of the oxide,[28,29,32−39] apparently ruling out copper-induced *p*-type conductivity.

The optoelectronic properties of Cu-doped ZnO have also caused great interest in the scientific community. The seminal work of Dingle in 1969 showed intense emission peaked at 2.48 eV in samples bearing copper, advancing Cu as a viable source for green luminescence (GL).[29] This prompted a large number of subsequent studies that confirmed and expanded these findings (e.g., refs 39 and 41). Furthermore, a lively and ongoing debate about the origin of the emission spectrum has been ignited.[32,33,42,43] The mechanism primarily proposed by Dingle[29] describes GL as a two-step mechanism initiated by the reduction of Cu^{2+} to Cu^{+}, due to a photogenerated electron, and subsequent recombination with a hole at a shallow acceptor level. Such an interpretation, seemingly

Received: October 10, 2025
Revised: January 5, 2026
Accepted: January 20, 2026
Published: February 3, 2026

https://doi.org/10.1021/acs.energyfuels.5c05337
Energy Fuels 2026, 40, 3397−3407

supported by calculations and measurements suggesting the occurrence of a Cu-related acceptor level below the edge of the ZnO conduction band[33,36,39,44] has long been unquestioned. However, alternative explanations based on novel experimental and theoretical results have recently challenged this view.[32,42,43] In particular, the involvement of the Cu^{3+} oxidized state has been hypothesized either as the final state of the GL process[43] or as the state undergoing recombination with a free electron at the defect site.[32] Complex defect states have also been invoked to interpret the experiment but it has been argued that they should be excluded on the basis of symmetry considerations.[33]

Nowadays, one of the major current research directions for Cu-doped ZnO involves its possible application in heterogeneous photocatalysis.[17,18] In fact, ZnO band edges are suitably aligned with respect to the redox potentials of the water-splitting reaction, namely the reduction of $H^+(aq)$ to $H_2(g)$ and the $H_2O(l)$oxidation reaction to $O_2(g)$.[19,20] This, in addition to its straightforward deposition on inorganic and organic substrates (e.g., via atomic layer deposition[45−47]), renders ZnO a useful additive in photocatalytic devices, as it shields the light absorber from corrosion, enhances charge separation, and facilitates redox reactions at the solid−liquid interface.[48−52] In this context, moderate inclusion (typically 1−5 at %) of Cu in the oxide has been found to boost their activity toward both photoreduction and photooxidation processes, whereas unsatisfactory performances are recorded at higher concentrations.[53−57] Furthermore, Cu-doped ZnO is water-stable, as evidenced by reusability studies showing robust performance over multiple catalytic cycles and minimal copper loss.[58−60] It has been suggested that the superior performances of doped ZnO may ensue from improved optoelectronic properties (e.g., reduced charge recombination) and direct catalytic effects (i.e., promotion of radical formation at the heterogeneous interface).[53−57] Nevertheless, an in-depth mechanistic explanation of Cu role in augmenting the photocatalytic efficiency of ZnO is still lacking.

Overall, definitive answers to the open questions just outlined are intimately related to the identification and appropriate description of the Cu defect states in bulk ZnO and at its relevant surfaces. Emission channeling measurements indicate that 60−70% of the copper embodied in ZnO occupies the ideal Zn lattice site.[61] For this reason, substitutional copper, Cu_{Zn}, has been linked with the spectroscopic features[29,39,44] and has been modeled in several computational studies.[30−37] The calculated energy levels attributed to Cu_{Zn} span a broad interval in the literature, largely depending on the adopted level of theory.[30−33,35−37] For example, the acceptor level, related with the capture of an extra electron on the neutral defect site [i.e., reduction of Cu^{2+} ($3d^9$) to Cu^+ ($3d^{10}$)] has been predicted to lie between 0.7 and 4.40 eV above the valence band maximum (VBM) of ZnO.[30−33,35−37] In view of the band gap of ZnO (3.44 eV), different physical interpretations are achieved, as levels above the conduction band minimum (CBM) indicate that the defect should be electronically inert. Further, the occurrence of a donor level [i.e., oxidation to Cu^{3+} ($3d^8$)] has been reported, with values ranging between 0.36 and 1.14 eV above the VBM,[31,32,37] and has been related with GL.[32] In addition to Cu_{Zn}, the interstitial defect Cu_i might be (at least partially) responsible for the observed optoelectronic and photocatalytic properties. In fact, although largely overlooked, Cu_i may still represent a significant fraction of Cu assimilated in the oxide,[61] particularly under O-poor conditions.[37] Finally, in stark contrast with bulk properties, Cu energy levels at the surface of ZnO have received far less attention, with most of the current studies focusing on clustering and Cu overlayers on the surface rather than analyzing the effect of copper in the doping regime.[62−64]

In the present article, we employ advanced electronic-structure calculations to investigate the energetics and electronic properties of Cu_{Zn} and Cu_i in bulk ZnO and at its relevant $(10\bar{1}0)$ surface. We first show that substitutional Cu in ZnO behaves as a deep donor but cannot accept electrons. Moreover, the defect levels of Cu_i lie either deep (acceptor) or below (donor) the VBM of ZnO. This explains why achieving *p*-type conductivity through Cu doping is highly unlikely. The optical response of Cu-doped ZnO, principally the characteristic green luminescence, is consistent with donor-related transitions involving Cu_{Zn}, at variance with earlier interpretations based on shallow acceptor states of the defect. Then, our study of Cu defects at the surface of ZnO unveils striking differences if compared with the bulk, mainly (i) surface Cu_{Zn} displays both donor and acceptor levels, and (ii) interstitial Cu^{2+} ions are remarkably stabilized when adsorbed on the surface and favored over substitutional Cu in a wider range of conditions. Alignment of the Cu energy levels and redox potentials of aqueous species at the semiconductor-water interface reveals that surface Cu_{Zn} can facilitate electron and hole transfer to aqueous species, supporting both reduction and oxidation in the global water-splitting reaction, whereas surface Cu_i is largely inactive toward electron transfer and only partially aligned for hole injection under alkaline conditions. These findings explain the experimental trends showing better performances for ZnO samples with low Cu content and suggest that the balance between substitutional and interstitial surface defects governs the photocatalytic efficiency of Cu-doped ZnO, with substitutional Cu playing the primary role at low concentrations of the dopant.

The article is organized as follows: in Section 2 we present the theoretical formulation employed to calculate the formation energies of Cu defects in ZnO; in Section 3, we report the computational details of the performed electronic-structure calculations; in Sections 4 and 5, we discuss the results obtained on Cu doping for bulk ZnO and for the apolar $(10\bar{1}0)$ surface, respectively. The conclusions are drawn in Section 6.

2. THEORY

To properly describe the energetics and the electronic properties of Cu-related defects in ZnO from first-principles, it is mandatory to accurately evaluate the respective formation energies. To this end, here we employ the grand-canonical formulation of defects in crystalline materials[65,66] which has been also extended to the study of solutes in aqueous solution and adsorbates at the solid−liquid interface.[67−69] Within this theory, the formation energy of a defect X with charge q in the relaxed nuclear coordinates R_q, $E_f[X^q(R_q)]$, reads as[65,66,70]

$$E_f[X^q(R_q)] = E[X^q(R_q)] - E[\text{bulk}] + \sum n_i\mu_i + q(\epsilon_v + \mu_e) + E_{corr}[X^q(R_q)] \quad (1)$$

where $E[X^q(R_q)]$ is the total energy of a periodic supercell of the host material, containing a single defect $X^q(R_q)$, $E[\text{bulk}]$ the total energy of the pristine bulk supercell. The term $\epsilon_v + \mu_e$,

https://doi.org/10.1021/acs.energyfuels.5c05337
Energy Fuels 2026, 40, 3397−3407

including the VBM of the perfect crystal and the electron chemical potential, respectively, represents the electron reservoir, required by the grand-canonical ensemble when dealing with charged defects (i.e., $q \neq 0$). Similarly, μ_i is the chemical potential of the species i added/subtracted from the supercell n_i times. $E_{corr}[X^q(R_q)]$ is a correction term, which applies to the total DFT energy of charged supercells that carry a localized electron density, and eliminates spurious electrostatic interactions between periodic replicas.[65,66,71] We adopt the Freysoldt−Neugebauer−Van de Walle (FNV) scheme[65,66] which defines this term as the model correction for a charge q screened by a static dielectric constant ε_0:

$$E_{corr}(q, R_q) = E_m(q, \varepsilon_0) \tag{2}$$

We here use the measured value for ZnO, $\varepsilon_0 = 9.3$.[72] The calculated correction terms for the supercell employed in this study are given in Table S1 of the Supporting Information (SI).

Therefore, the formation energies of the substitutional and interstitial Cu defects in ZnO are given, respectively, as

$$E_f[Cu^q_{Zn}(R_q)] = E[Cu^q_{Zn}(R_q)] - E[ZnO] + q[\epsilon_v(ZnO) + \mu_e] + \mu_{Zn} - \mu_{Cu} + E_{corr}[Cu^q_{Zn}(R_q)] \tag{3}$$

$$E_f[Cu^q_i(R_q)] = E[Cu^q_i(R_q)] - E[ZnO] + q[\epsilon_v(ZnO) + \mu_e] - \mu_{Cu} + E_{corr}[Cu^q_i(R_q)] \tag{4}$$

From eqs 3 and 4, it is evident that the formation energies of Cu defects depend on the chemical potential of the constituting elements of ZnO and of the dopant. The values that these quantities can assume are bound by the thermodynamic stability condition of the host material:

$$\Delta H_f(ZnO) = \Delta\mu_{Zn} + \Delta\mu_O \tag{5}$$

where $\Delta H_f(ZnO)$ is the formation enthalpy of ZnO, $\Delta\mu_{Zn}$ and $\Delta\mu_O$ represent the deviations of μ_{Zn} and μ_O chemical potentials from their standard states, which, in turn, give the following upper bound limits:

$$\Delta\mu_{Zn} = \mu_{Zn} - \mu^0_{Zn} \leq 0 \tag{6}$$

$$\Delta\mu_O = \mu_O - \mu^0_O \leq 0 \tag{7}$$

In eqs 6 and 7, μ^0_{Zn} is defined as the total energy per atom of metallic zinc and μ^0_O is the energy of O in the O_2 molecule. Both are here calculated with DFT calculations (cf. Section 3). Zn-rich/O-poor conditions correspond to $\Delta\mu_{Zn} = 0$, i.e., $\mu_{Zn} = \mu^0_{Zn}$. Therefore, from eq 5, $\Delta\mu_O = \Delta H_f(ZnO)$; conversely, O-rich/Zn-poor conditions with $\Delta\mu_O = 0$, entail $\Delta\mu_{Zn} = \Delta H_f(ZnO)$. Stoichiometric Zn/O-intermediate conditions can be simulated by taking the values at the midpoint of the ZnO stability region, i.e., $\Delta\mu_{Zn} = \Delta\mu_0 = \Delta H_f(ZnO)/2$. The chemical potentials of Zn and O also constraint that of Cu, which must remain within values that do not ensue the formation of secondary phases. Therefore, the following additional inequalities must hold:

$$\Delta H_f(CuO) \geq \Delta\mu_{Cu} + \Delta\mu_O \tag{8}$$

$$\Delta H_f(Cu_2O) \geq 2\Delta\mu_{Cu} + \Delta\mu_O \tag{9}$$

$$\Delta H_f(ZnCu) \geq \Delta\mu_{Zn} + \Delta\mu_{Cu} \tag{10}$$

which set the boundaries against the formation of Cu oxides or of the intermetallic CuZn alloy, for O-rich and Zn-rich conditions, respectively, and complement the obvious upper bound given by Cu standard state, i.e., metallic copper:

$$\Delta\mu_{Cu} = \mu_{Cu} - \mu^0_{Cu} \leq 0 \tag{11}$$

All quantities required to estimate the chemical potentials of Zn, O, and Cu are here calculated from first-principles for consistency (cf. Section 3) and are reported in Section S2 of the Supporting Information along with the estimated $\Delta\mu_{Zn}$, $\Delta\mu_O$, and $\Delta\mu_{Cu}$ under O-rich/Zn-poor, O-poor/Zn-rich, and intermediate conditions, respectively.

Calculation of the formation energies at different charge states allows us to determine the adiabatic energy levels connected with the capture/donation of one of more electrons by the defect. An adiabatic charge transition level (CTL) is formally defined as the value of the electron chemical potential at which $E_f[X^q(R_q)] = E_f[X^{q'}(R_{q'})]$:[65,66]

$$\mu^{ad}(X^q/X^{q'}) = \frac{E[X^q(R_q)] - E[X^{q'}(R_{q'})]}{q' - q} + \frac{E_{corr}(R_q, q) - E_{corr}(R_{q'}, q')}{q' - q} - \epsilon_v \tag{12}$$

Similarly, when dealing with vertical transitions, such as those that can be probed with optical measurements, in which the nuclear coordinates of the defect are preserved to those of the initial charge state, i.e., $E_f[X^q(R_q)] = E_f[X^{q'}(R_q)]$, we can define a vertical charge transition level:

$$\mu^{opt}_{q\to q'}(X^q/X^{q'}) = \frac{E[X^q(R_q)] - E[X^{q'}(R_q)]}{q' - q} + \frac{E_{corr}(R_q, q) - E_{corr}(R_q, q')}{q' - q} - \epsilon_v \tag{13}$$

where $\mu^{opt}_{q\to q'}$ denotes a vertical transition from q to q' at R_q fixed. In eq 13, $E_{corr}(R_q, q')$ is the finite-size correction of the supercell upon vertical variation of charge state. $E_{corr}(R_q, q')$ is here evaluated with the method developed in ref 71, which gives the following operative expression:[70,71]

$$E_{corr}(R_q, q') = E_m(q, \varepsilon_0) - E_m(q + q_{pol}, \varepsilon_\infty) + E_m(q' + q_{pol}, \varepsilon_\infty) \tag{14}$$

where ε_∞ is the high-frequency dielectric constant of the material (3.74 for ZnO[73]), q_{pol} is the ionic polarization charge, deriving from the response of the medium and defined as[71]

$$q_{pol} = -q\left(1 - \frac{\varepsilon_\infty}{\varepsilon_0}\right) \tag{15}$$

It is important to underline, from eq 14, that this term is not null for $q' = 0$, because of the ionic polarization charge, remaining in the neutral supercell, after vertical removal/injection of an electron.[70,71,74] The calculated values for electrostatic-finite correction of vertically reduced/oxidized systems are given in Table S1 of the Supporting Information.

https://doi.org/10.1021/acs.energyfuels.5c05337
Energy Fuels 2026, 40, 3397−3407

The formulation presented here for the bulk is applied also to calculate the adiabatic energy levels at the surface of ZnO. The sole key difference lies in the method employed to correct the electrostatic finite-size error arising for a charged point defect at the surface of the periodic slab. In this case, we utilize the method specifically developed by Komsa and Pasquarello to account for the varying dielectric profile across the semiconductor-vacuum interface.[75] The correction is defined as[75]

$$E_{\mathrm{corr}}^{\mathrm{slab}}(R_q, q) = E_{\mathrm{iso}} - E_{\mathrm{per}} + q\Delta V \tag{16}$$

where E_{per} is the electrostatic energy modeled for the periodic supercell, E_{iso} that of the isolated charge assuming uniform scaling of all the three dimensions of the supercell (including the vacuum layer), and ΔV an alignment term accounting for the shift between model and DFT potentials.[75]

3. COMPUTATIONAL METHODS

All density functional theory (DFT) calculations presented in this article are carried out with the freely available CP2K-QUICKSTEP suite of codes.[76−78] We employ Goedecker−Teter−Hutter pseudopotentials[79] for core electrons and we use MOLOPT double-ζ polarized basis set[77] for valence electrons, both explicitly designed for hybrid functionals.[78] A cutoff of 600 Ry is set for the plane waves. Hybrid functionals calculations are carried out at a reasonable cost by taking advantage of the auxiliary density matrix method,[80−82] as available in CP2K. We make use of the cFIT auxiliary basis set,[82] which entails both accuracy and affordable computational time.[74] Calculations involving unpaired electrons are performed adopting the unrestricted Kohn−Sham formalism and, in some cases, specifying the desired system multiplicity (*vide infra*).

Our choice for the density functional is guided by the need to neutralize the self-interaction error, typical of standard DFT methods, which would cause an incorrect description of charge localization in semiconductors.[83,84] For this reason, we employ a piecewise linear (PWL) hybrid functional belonging to the PBE0[85,86] family. The fraction of Fock exchange to be included in this global hybrid functional has been determined in refs 87 and 88 from the fulfillment of the generalized Koopman's condition and was calculated to be equal to 25% for ZnO (i.e., in this particular case, equivalent to the original PBE0 formulation[85,86]). This functional somewhat underestimates the band gap of ZnO (3.13 in ref 88, 3.20 eV in this study, to be compared with 3.44 eV[21]). In order to preserve the quality of the electronic structure achieved with the PWL functional, while avoiding its band gap error, we refer (i.e., via the average electrostatic potential) the PWL energy levels against the VBM and CBM of ZnO, as obtained when tuning the fraction of Fock exchange to reproduce the experimental band gap.[19,20] This can be safely performed, as it has been demonstrated that the position of charge transition levels is robust against the fraction of Fock exchange included in the global hybrid functional, as long as the band gap is not too largely underestimated.[67,74,89,90]

In Table S2, we report the structural parameters of the supercells employed to simulate bulk ZnO, along with those of metallic Cu, Zn, Cu_2O, CuO and CuZn, required to define the chemical potential of Zn, O and Cu (cf. Section 2 and Table S2 of Supporting Information). For CuO, we calculate the antiferromagnetic ground state.[91] For all these materials, we perform structural relaxations of the nuclei, while the lattice vectors are kept fixed to those of the experimental references. In addition, we calculate the total energy of the isolated O_2 molecule, again at the hybrid functional level, to avoid the unsatisfactory description of the ground-state triplet, typical of standard DFT methods.

In Figure 1a,b, we illustrate the 4 × 4 × 3 supercell (192 atoms) employed to simulate bulk ZnO and highlight the positions of the studied Cu defects. For Cu_i we consider insertion of copper in the octahedral cavity of ZnO, which was predicted to be by far the most stable site for Zn interstitials in previous DFT studies.[23] Analogously, in Figure 1c, we depict the slab employed to model the ZnO-vacuum interface. We here consider the stable apolar $(10\bar{1}0)$ surface[92,93] and construct a 144-atoms orthorhombic slab with a = 10.40 Å, b = 9.66 Å, and c = 46.73 Å, the latter including a 30.0 Å layer of vacuum, which ensures that the computations are not affected by spurious interactions among periodic replicas (cf. Figure S1 for plane-averaged electrostatic potential of the slab). The Cu concentrations used in our calculation are 3.86×10^{20} atoms/cm^3 (1.04 at %) and 9.95×10^{13} atoms/cm^2 (1.4 at %) in the bulk and in the slab ZnO structures, respectively. Such a setup was found to provide well-converged electronic properties in previous studies.[19,20] For modeling defects in the slab, see Figure 1c, we test three sites for Cu_{Zn}: substitution on (i) a undercoordinated surface Zn, (ii) a subsurface Zn, and (iii) a bulk-like site. In a similar fashion, we model Cu_i by inserting an extra Cu into surface and subsurface and bulk-like cavities.

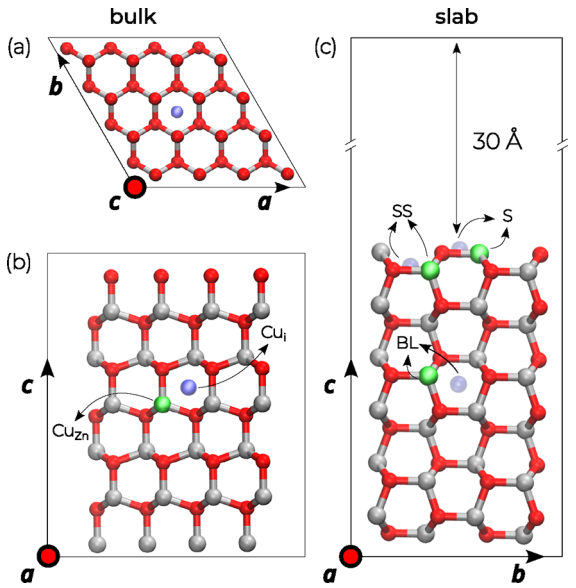

Figure 1. Stick-and-ball representation of the hexagonal supercell (a = b = 12.88 Å, c = 15.60 Å) employed to model bulk ZnO [panels (a) and (b)] and of the orthorhombic slab (a = 10.40 Å, b = 9.66 Å, and c = 46.73 Å) employed to model the apolar $(10\bar{1}0)$ surface [panel (c)]. Zinc in gray, oxygen in red. Atoms highlighted in green and faded blue represent the substitutional Cu doping sites and the positions in which an extra Cu has been inserted to simulate the interstitial defect, i.e., surface (S), subsurface (SS), and bulk-like (BL).

4. CU DOPING IN BULK ZNO

We first discuss the modeling of Cu incorporation in bulk ZnO. In Table 1, for clarity, we schematize the electronic structure of Cu defects in the various charge states. For the substitutional defect, we perform calculations on three charge states q = +1, 0, −1: the charge-neutral substitution, i.e., Cu_{Zn}^0 corresponding to Cu^{2+} ($3d^9$) and the respective oxidized (q = +1) and reduced (q = −1) states. Similarly, for Cu_i^q, we simulate the analogous defect charge states entailing the same electronic configurations of Cu, i.e., q = +3, +2, +1. We do not include in the discussion neither Cu_{Zn}^{-2} nor Cu_i^0, both representing atomic Cu, as the 4s orbital is much above the CB of ZnO and hence unable to accept an electron.

For the substitutional defect, the charge-neutral Cu_{Zn}^0, shown in Figure 2a, displays three equal Cu−O bonds of 1.98 Å and a shorter one of 1.91 Å along the c axis. This is consistent with a local symmetry reduction from T_d, typical of Zn in wurtzite ZnO, to C_{3v}, induced by the Jahn−Teller distortion of Cu^{2+}.

https://doi.org/10.1021/acs.energyfuels.5c05337
Energy Fuels 2026, 40, 3397−3407

Table 1. Details of the Cu Defects Studied in This Work: Formal Charge q, Formal Ionic Charge and Electronic Configuration of Cu in the Supercell, and Spin Multiplicity of the System (S for Singlet, D for Doublet, and T for Triplet), cf. Main Text for More Details[a]

defect	Cu^{q}_{Zn}			Cu^{q}_{i}		
q	+1	0	−1	+3	+2	+1
ionic charge	$Cu^{2+} + h^{+}_{loc}$	Cu^{2+}	Cu^{+} [$Cu^{2+} + e^{-}$(CB)]	$Cu^{2+} + h^{+}_{loc}$	Cu^{2+}	Cu^{+}
configuration	$3d^9$	$3d^9$	$3d^{10}$ [$3d^9 + e^{-}$(CB)]	$3d^9$	$3d^9$	$3d^{10}$
spin multiplicity	T	D	S (T)	T	D	S

[a]For Cu^{-1}_{Zn}, we consider, in addition to the d^{10}/Cu^{+} defect, also a state in which an extra electron is added to the conduction band of ZnO (in parentheses), cf. main text.

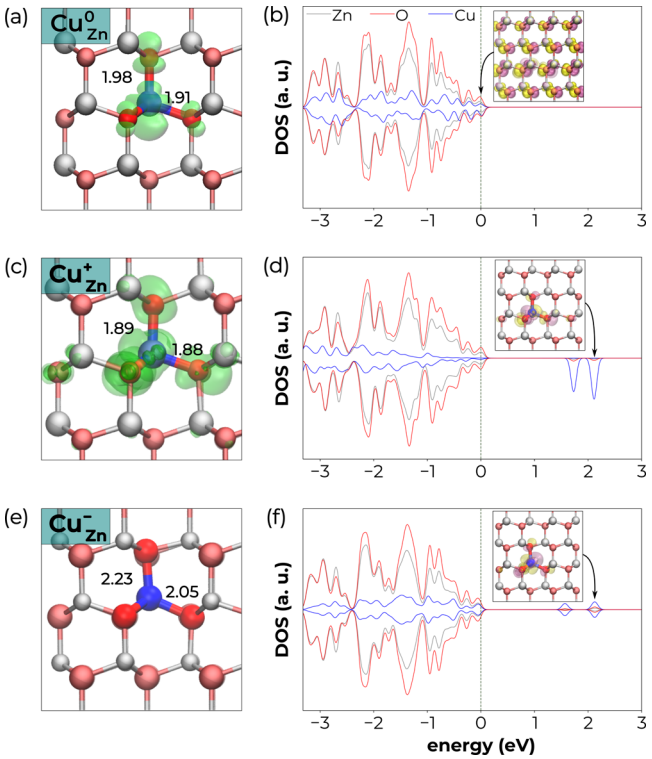

Figure 2. Stick-and-ball representation of Cu^{q}_{Zn} for neutral [q = 0 panel (a)], oxidized [q = +1, panel (c)], and reduced species [q = −1, panel (e)], highlighting the relevant Cu−O bond lengths (given in Å). Zn in gray, O in red, and Cu in blue. The respective isodensity representation (isovalue: 0.001 au) of the spin density is included where appropriate (cf. main text). Projected electronic densities of states for each system are given in panels (b), (d), and (f), including both spin populations. The contributions of Cu to the DOS are artificially enhanced for the purpose of the presentation. Insets of the panels include isodensity representations of either the singly highest occupied molecular orbitals (for Cu^{0}_{Zn} and Cu^{-}_{Zn}) or the lowest unoccupied molecular orbital (for Cu^{+}_{Zn}).

The localized spin density is consistent with the doublet spin multiplicity expected for a $3d^9$ configuration. We note that it protrudes toward the coordinating oxygen atoms, denoting a certain degree of Cu−O hybridization. Interestingly, inspection of the electronic density of states as well as of the highest occupied and lowest unoccupied molecular orbitals (cf. Figure 2b) reveals that neutral Cu substitution does not induce any localized state within the gap of the oxide, as Cu 3d states are resonant with those of the host material.

Next, we focus on Cu^{+1}_{Zn}, i.e., formally oxidation to d^8 Cu^{3+}. As a matter of fact, injection of an extra hole alleviates the Jahn−Teller distortion, as we find all the oxygen atoms relaxing toward the central Cu, with bond lengths comprised between 1.88 and 1.90 Å, see Figure 2c. We notice both spin localization, ensuing from the triplet state, *and* a localized energy level above the VBM of ZnO, which is congruous with stabilization of the hole upon electron detachment, cf. Figure 2c,d. Such a triplet electronic configuration is found to be 1.11 eV more stable than the corresponding singlet, consistent with the strong Cu character of the associated state (as Hund's rules dictates that d^8 Cu^{3+} should be more stable as a triplet). Nevertheless, closer inspection of the spin moment reveals that 54% of it is localized on Cu (to be compared with 87% estimated for the Cu^{0}_{Zn}), whereas the remaining 46% is distributed among O first neighbors. This suggests that d^9 Cu^{2+} is somewhat preserved in the Cu^{+}_{Zn} defect. Therefore, the injected hole is mainly localized (h^{+}_{loc}, cf. Table 1) on the surrounding O atoms, in a fashion similar to that observed in coordination complexes.[94]

Finally, we move on the reduced Cu^{-1}_{Zn} species, for which we observe a marked elongation of all bond lengths, when compared to the neutral case, − up to ≈0.25 Å for the axial Cu-bond − generated by the filling of antibonding orbital. This is accompanied by electron localization on the CuO_4 moiety, see Figure 2e,f. However, we note that the singlet state of Cu d^{10} is not the most stable configuration for the negatively charged supercell. In fact, we find the triplet state to be more stable by as much as 0.59 eV. In the latter, the extra electron does not fill the 3d of Cu^{2+} but is assimilated in the conduction band edge of ZnO, i.e., the system modeled is actually Cu^{0}_{Zn} + e^{-}(CB) rather than Cu^{-1}_{Zn}. This is confirmed by observation of the structural features and the localized spin density, which are close to those of Cu^{0}_{Zn}, cf. Figure S2. Furthermore, the DOS is devoid of any in-gap state and the highest singly occupied molecular orbital (SOMO) is completely delocalized, Figure S2, corresponding to the bottom of the ZnO CB. This hints at the possibility that substitutional Cu may *not* really accept electrons.

For the interstitial Cu, Cu^{+2}_{i}, i.e., the d^9 ion, relaxation upon insertion in the octahedral site (see Figure 1) causes a conspicuous rearrangement of the cavity accommodating the defect. This results in large outward displacements of Zn atoms as Cu coordinates six lattice O atoms in a highly distorted octahedron, see Figure 3a with bond lengths ranging from 1.98 to 2.33 Å. At variance with Cu^{0}_{Zn}, the system has an energy level very close to the VB, corresponding to a semilocalized state, cf. Figure 3b. As done previously, we then consider possible oxidation (Cu^{+3}_{i}) and reduction (Cu^{+}_{i}) of the defect: in addition to distortions affine to those displayed by the interstitial − i.e., shrinking and elongation of Cu−O bonds, respectively − we note a remarkable reorganization of the cavity adjusting for the different charge state, particularly in the case of Cu^{+}_{i}, see Figure 3c,e. We also individuate in-gap states,

https://doi.org/10.1021/acs.energyfuels.5c05337
Energy Fuels 2026, 40, 3397−3407

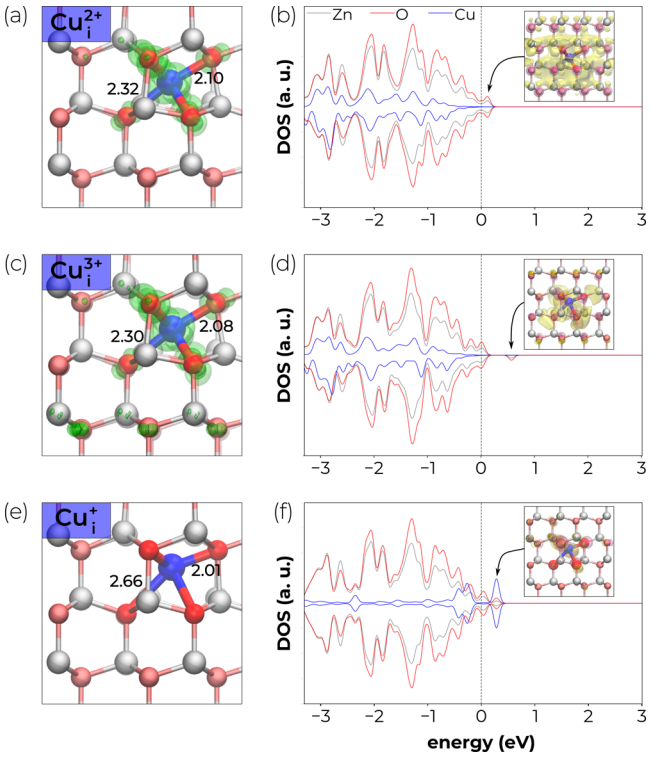

Figure 3. Stick-and-ball representation of Cu_i^q for q = +2 (a), for the oxidized [(q = +3, panel (c)], and reduced species [q = +1, panel (e)], highlighting the relevant Cu−O bond lengths (given in Å). Zn in gray, O in red, and Cu in blue. The respective isodensity representation (isovalue: 0.001 au) of the spin density is included where appropriate (cf. main text). Projected electronic densities of states for each system are given in panels (b), (d), and (f), including both spin populations. The contributions of Cu to the DOS are artificially enhanced for the purpose of the presentation. Insets of the panels include isodensity representations of either the singly highest occupied molecular orbitals (for Cu_i^{+2} and Cu_i^{+}) or the lowest unoccupied molecular orbital (for Cu_i^{3+}).

with Cu_i^{+} exhibiting a pronounced localization on the impurity whereas the oxidized Cu_i^{3+} presents a diffuse electron density, in line with a higher degree of hybridization with the host states, cf. Figure 3d,f.

In Figure 4a−c, we report the formation energy diagrams for Cu_{Zn}^q and Cu_i^q. Our results reveal a clear competition between the substitutional and interstitial defects, with the former being favored in O-rich conditions, whereas a higher concentration of the interstitial may be expected when Zn-rich samples are achieved, e.g., after annealing or following a postgrowth vacuum/reducing treatment.[61] Interestingly, intermediate conditions should still favor the substitutional, notwithstanding the sizable drop in formation energy for the interstitial. Still, for a typical n-type ZnO, the neutral substitution represents, by far, the Cu defect with the lowest formation energy (and hence the most abundant), regardless of the conditions. However, for samples in which the Fermi level is pinned deeper in the gap of the material, the interstitial defect, as Cu_i^{2+}, displays formation energies comparable to those of Cu_{Zn}^0. This suggests that the copper incorporated in the oxide should be more evenly distributed among lattice and interstitial sites. Finally, for a p-type oxide, the interstitial defect should dominate for a wide range of chemical potentials, except those associated with extreme oxygen abundance.

The calculated adiabatic CTLs, cf. Figure 4d, indicate that substitutional Cu may only act as deep donor, i.e., losing a e^- in the oxidation process $Cu_{Zn}^0 \rightarrow Cu_{Zn}^+ + e^-$ and *cannot* accept electrons. In fact, it presents $\mu^{ad}(Cu_{Zn}^+/Cu_{Zn}^0)$ at 0.49 eV above the VB of ZnO, while the donor level $\mu^{ad}(Cu_{Zn}^0/Cu_{Zn}^-)$ falls 0.51 eV deep within the CB of the oxide, ruling out any capability of capturing electrons. At variance with this, for the interstitial, we calculate (i) a donor level $\mu^{ad}(Cu_i^{+3}/Cu_i^{+2})$ = 2.21 eV, pointing to electron-trapping properties of the defect, and (ii) an acceptor level, $\mu^{ad}(Cu_i^{3+}/Cu_i^{2+})$, 0.35 eV below the VBM of ZnO, excluding oxidation of the interstitial Cu.

In Figure 4d, we report the vertical energy levels, which can be related with the optical transitions measured in absorption and emission spectra of Cu-doped ZnO. The physical picture resulting from our computational analysis is schematized with the configuration coordinate diagrams given in Figure 4e,f, for the substitutional and interstitial defects, respectively. Since Cu_{Zn}^0 cannot be reduced, we consider the optical processes for the (+1/0) couple, for which we calculate $\mu_{0\rightarrow1}^{opt}$ = 0.07 eV and $\mu_{1\rightarrow0}^{opt}$ = 1.06 eV, respectively. The substantial dissimilarity between vertical and adiabatic levels derives from the prominent difference in the equilibrium structures of the defects in the neutral and positive charge states. Then, the GL of Cu-doped ZnO can be rationalized assuming a two-step process composed by (i) photo-oxidation of Cu_{Zn}^0 to Cu_{Zn}^+, (ii) subsequent radiative recombination with a photogenerated e^- in the CB of ZnO, i.e., vertical reduction (cf. Figure 4e). From the calculated values of $\mu_{1\rightarrow0}^{opt}$ and $\mu_{0\rightarrow1}^{opt}$ and the band gap of ZnO (3.44 eV), we infer an energy of 3.37 eV for the vertical excitation of an electron from Cu_{Zn}^0 into the CB, while recombination should occur with emission at 2.35 eV, cf. Figure 4e. The latter value is in very good agreement with the position of the measured PL peak, ranging from 2.39 to 2.48 eV,[29,39,41] thus corroborating the validity of our approach. At variance with this, spectroscopic signatures of the interstitial may be detected considering (i) photoreduction Cu_i^{2+} to Cu_i^{+} upon excitation of an electron from the VB and (ii) oxidation of Cu_i^{+} with a photogenerated hole, with corresponding $\mu_{2\rightarrow1}^{opt}$ = 3.17 eV and $\mu_{1\rightarrow2}^{opt}$ = 0.65, respectively, cf. Figure 4d,f, possibly linked with UV and infrared signals in Cu-doped samples.[1]

We conclude this section by discussing the present findings in the context of previous studies on the subject. The defect physics emerging from our modeling consolidate the view that p-type ZnO may hardly be obtained through Cu doping.[1] We note that the Cu interstitial has a (+3/+2) CTL slightly below the valence-band maximum of ZnO. This suggests that, in principle, p-type conductivity could still be attained, if the transition level is shifted by complex defect formation (for example with native defects or impurities). However, interstitial Cu is favored in Zn-rich conditions, where compensating defects, such as the O vacancy and Zn interstitial, are abundant.[23]

Concerning the optical properties, we provide robust evidence to support the GL mechanism of Cu-doped ZnO involving a deep donor state, originally proposed in ref 32. However, differently from ref 32, in which the Dingle mechanism was ruled out on the basis of a discrepancy between acceptor levels and the experiment, we here assert that, actually, Cu_{Zn} cannot accept electrons, as the related CTL falls in the CB of ZnO, in line with a recent study.[37] This finding contrasts with earlier assignment of an acceptor state for Cu_{Zn} at ≈0.2 eV below the CB of ZnO, based on admittance spectroscopy.[44] However, we note that alternative

https://doi.org/10.1021/acs.energyfuels.5c05337
Energy Fuels 2026, 40, 3397−3407

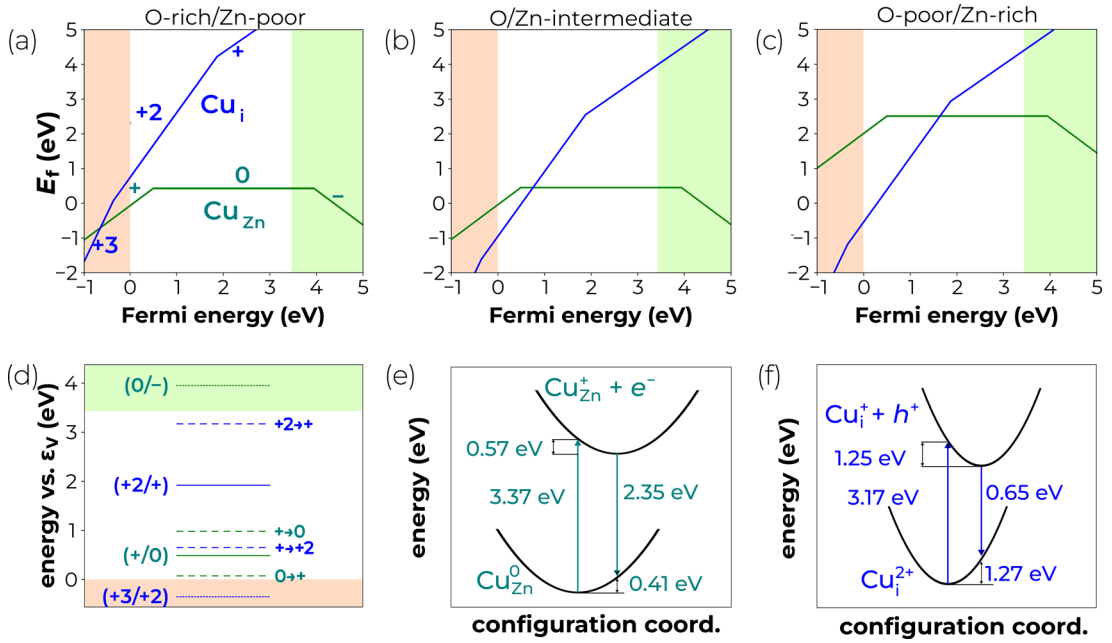

Figure 4. Formation energies of substitutional and interstitial Cu in bulk ZnO, as calculated for (a) O-rich/Zn-poor, (b) intermediate, and (c) O-poor/Zn-rich conditions. Adiabatic and vertical CTLs (d). Calculated configuration coordinate diagrams for Cu_{Zn} and Cu_i in ZnO [panels (e) and (f), cf. main text].

explanations to the signal may involve either native defects, hydrogen impurities, usually present in ZnO samples,[23] or Cu defect complexes. Furthermore, interface/surface traps (vide infra) may appear as shallow levels close to the CB edge.[1]

5. CU DOPING ON THE (10$\bar{1}$0) SURFACE OF ZNO

Having demonstrated that our approach allows for an accurate characterization of the bulk Cu defects, we next examine the physics of Cu defects at the stable, apolar (10$\bar{1}$0) surface, cf. Figure 1c, with a clear focus on the consequences of our investigation for the photocatalytic applications of Cu-doped ZnO. For the neutral Cu^0_{Zn}, the tricoordinated Cu^{2+} ion has two equal Cu−O bonds with a length of 1.90 Å and a shorter 1.84 Å bond, cf. Figure 5a. Similarly to the bulk case, upon

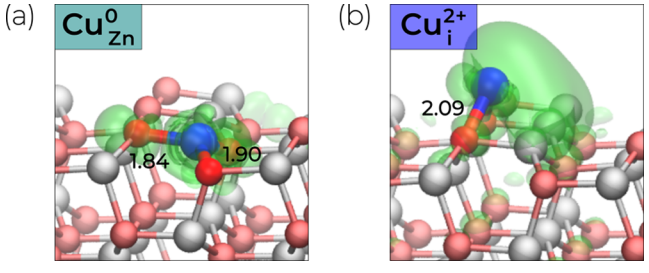

Figure 5. Stick-and-ball representation of (a) Cu^0_{Zn} and (b) Cu^{2+}_i, highlighting the relevant Cu−O bond lengths (given in Å). Zn in gray, O in red, and Cu in blue, along with the isodensity representation (isovalue: 0.001 a. u.) of spin densities.

oxidation to Cu^+_{Zn}, we observe a slight shortening (≈0.02 Å) of all the Cu−O bond lengths while the reduced Cu^-_{Zn} shows a sizable elongation (up to 2.27 Å), as a consequence of the depletion/filling of antibonding orbital, cf. Figure S3. We pinpoint that, also for slab calculations, we have considered the triplet spin state for the $q = -1$ supercell: in this case, the latter is calculated to be 0.72 above in energy with respect to the singlet, which ensures that d^{10} Cu^+ is the true ground state for the $q = -1$ supercell.

To understand the stability of Cu_{Zn} at (10$\bar{1}$0) surface of ZnO, we compare the total energies of the neutral defects inserted on surface, subsurface and bulk-like sites, cf. Figure 1c and Table S5. We find the slab having the substituent Cu in its bulk-like region to be the most stable by at least 0.63 eV. This suggests that concentration of Cu_{Zn} on the surface might be lower than that in the inner bulk region of the material. However, we note that Cu insertion on an under-coordinated surface Zn site is energetically favored over the subsurface substitution by as much as 0.40 eV, indicating that surface copper may be readily available to form bonds with aqueous species at the heterogeneous interface.

In contrast, when considering interstitial Cu^{2+}_i, there is a smaller difference (0.167 eV, see Table S5) for insertion on a surface or a subsurface site. This is due to the fact that, in both cases, Cu does not remain in the original position, Figure 1c, but instead raises above the surface plane and bridges two O atoms with Cu−O bond lengths of 2.09 Å, cf. Figure 5b, signifying that the system should be described as an adsorbed ion. Comparison with the total energy of the Cu^{2+}_i defect in the bulk-like region of the slab (Table S5) reveals that the surface Cu is more stable by as much as 1.65 eV. Again, we consider possible oxidized (Cu^{3+}_i) and reduced (Cu^+_i) defects. For the former, we see bond elongation (up to 0.04 Å), i.e., weakening of Cu−O interactions as copper becomes less positive and a partial localization of electron density on the interstitial, cf. Figure S3. Contrariwise, for the latter, Cu−O bonds are sensitively shortened (up to almost 0.1 Å), in virtue of the enhanced Cu ionic charge.

Building on this preliminary analysis, we hence focus on the formation energies and CTLs for the surface substitutional and interstitial defects, which are evaluated within the same theoretical framework detailed in Sections 2 and 4 but considering the pristine (10$\bar{1}$0) slab as our reference system. The formation energy diagrams, depicted in Figure 6, unveil a

https://doi.org/10.1021/acs.energyfuels.5c05337
Energy Fuels 2026, 40, 3397−3407

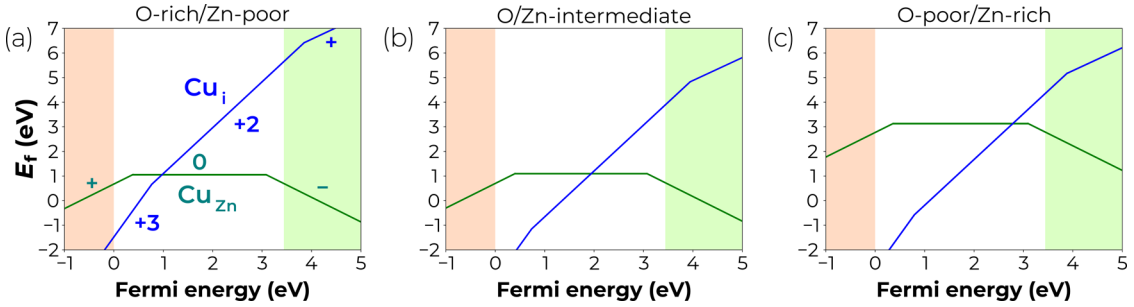

Figure 6. Formation energies of substitutional and interstitial Cu on the $(10\bar{1}0)$ surface of ZnO, as calculated for (a) O-rich/Zn-poor, (b) intermediate, and (c) O-poor/Zn-rich conditions.

striking difference with respect to the bulk with a general stabilization of the interstitial over the substitutional. Though O-rich/Zn-poor conditions should be dominated by the substitutional defect throughout a large span of Fermi energies, both intermediate and O-poor/Zn-rich see a remarkable shift toward the inclusion of Cu on the surface of ZnO as a bridging interstitial.

As far as the energy levels are concerned, surface Cu_{Zn} displays both a donor *and* an acceptor state, at 0.36 and 3.11 eV above the VB, respectively, cf. Figure 7, in contrast with

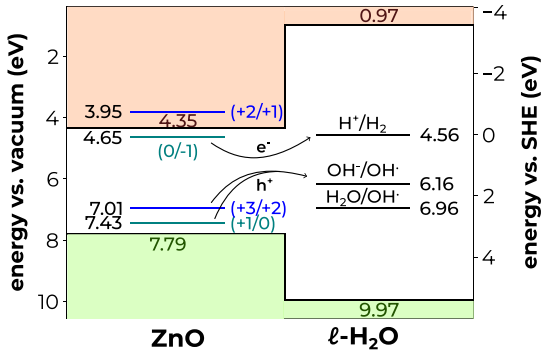

Figure 7. Valence band (VB) and conduction band (CB) edges of ZnO aligned with the band edges of liquid water and with the redox levels associated with the reduction of aqueous protons and the oxidation of water and aqueous hydroxide. Energies are reported vs both the vacuum level and the computational SHE of refs 67 and 95. Adiabatic charge transition levels of surface defects in the band gap of ZnO are included in the energy diagram (green for Cu_{Zn} and blue for Cu_i). Values inside the diagram, close to each level, refer to the alignment with respect to vacuum.

what has been observed for the bulk. The latter is consistent with a state ≈0.2 eV below the CB of ZnO, as probed by admittance spectroscopy,[44] thus hinting at a possible surface nature of the measured energy level. Concerning the interstitial, we find that surface Cu_i^{2+} becomes inert toward the acceptance of electrons as $\mu^{ad}(Cu_i^{2+}/Cu_{Zn}^{+})$ CTL falls inside the CB of ZnO. At variance, the stabilization of the oxidized species at the surface lifts $\mu^{ad}(Cu_i^{3+}/Cu_{Zn}^{2+})$ 0.78 eV above the VBM of the oxide, cf. Figure 7.

We conclude this section discussing the obtained results in view of the measured photocatalytic activity of Cu-doped samples. In Figure 7, the band edges of ZnO are provided with respect to the vacuum level[19] and, for consistency, with the computational standard hydrogen electrode developed in refs 67 and 95, which is placed at 4.56 eV below the vacuum level, in excellent accord with the commonly accepted value proposed by Trasatti (4.44 eV).[96] In addition to the CTLs of Cu defects, the diagram contains the energy levels of aqueous species, namely (i) the H^+/H_2 redox potential and (ii) the redox level associated with the first step of the water oxidation reaction under either acidic ($H_2O/OH^{\cdot}$) or alkaline ($OH^-/OH^{\cdot}$) conditions. For the latter levels, we include the accurate computational estimates at 6.16 and 6.96 eV, respectively.[67,70] The presented alignment of energy levels reveals that surface Cu_{Zn} can facilitate both the reduction and oxidation processes of the overall water splitting reaction: in fact, the (+1/0) level lies well below those related with the oxidation of water and hydroxide to hydroxyl radical, while the H^+/H_2 redox level is predicted to be only 0.09 above the acceptor (0/−1) CTL of Cu_{Zn}. Therefore, both holes and electrons captured by the defect can be easily transferred to aqueous species. At variance with this, the surface Cu_i cannot capture electrons and its (+3/+2) donor level is suitably aligned only with the $OH^-/OH^{\cdot}$ redox potential, which limits the feasibility of hole transfer to alkaline solutions.

Also in view of the beneficial impact that charge localization on the surface is expected to have on photocatalytic processes at the water-semiconductor interface,[97−99] our analysis suggests that substitutional Cu doping at the surface of ZnO may be related with the boost in photoconversion efficiencies measured at low concentrations of the dopant.[53−57] At higher concentrations of the Cu, i.e., higher Cu chemical potentials, the dopant is more likely to be assimilated as Cu_i, as evidenced by the formation energy diagrams in Figure 6. However, surface Cu_i (i) cannot contribute to reduction processes, (ii) covers surface O sites that inhibit adsorption of protons, and (iii) is expected to have only a minor impact on water oxidation. Overall, the present results can rationalize the experimental trends for the efficiency of Cu-doped ZnO samples and show that the competition between substitutional and interstitial surface defects may be key in determining the photocatalytic activity of ZnO-based systems. We conclude remarking that the present discussion on the photocatalytic activity of Cu-doped ZnO is based on thermodynamic aspects, and, therefore, the occurrence of kinetic barriers in the reaction, and hence overpotentials, cannot be excluded. However, while not sufficient, a suitable alignment of the energy levels is indeed necessary for a good photocatalytic activity and will be complemented by mechanistic studies in future work.

6. CONCLUSIONS

In conclusion, we provided a comprehensive understanding of Cu defects in bulk ZnO and at its surface. In the bulk, substitutional acts as a deep donor but is unable to accept

https://doi.org/10.1021/acs.energyfuels.5c05337
Energy Fuels 2026, 40, 3397−3407

electrons, while interstitial Cu introduces levels either deep in the gap or below the valence band, explaining the difficulty of achieving *p*-type conductivity via Cu doping. The characteristic green luminescence of Cu-doped ZnO has been assigned to donor-related transitions of Cu_{Zn}, rather than shallow acceptor states. At the surface, notable differences emerge: substitutional Cu exhibits both donor and acceptor levels, whereas interstitial Cu is strongly stabilized as an adsorbed ion and should dominate at high Cu concentrations. Alignment of the energy levels at the semiconductor−water interface suggests that surface Cu_{Zn} can provide hot-spots to mediate both electron and hole injection toward aqueous species involved in the overall water-splitting reaction. On the other hand, surface Cu_i may be less beneficial or even detrimental for the photocatalytic activity of Cu-doped samples. These results rationalize experimental observations of enhanced photocatalytic performance at low Cu concentrations and highlight that the interplay between substitutional and interstitial surface defects is critical for the photocatalytic efficiency of Cu-doped ZnO. Natural continuation of the present work will involve the detailed inspection of the mechanistic aspects of photocatalytic processes on Cu-doped ZnO and the role of the surface defects in influencing the overpotentials of the reactions.

■ ASSOCIATED CONTENT

Data Availability Statement

All the relevant data (inputs, outputs) used to produce the computational results presented in this work are available at the following public repository: https://github.com/Michi12Michi/Cu-ZnO-Supporting-data.

Supporting Information

The Supporting Information is available free of charge at https://pubs.acs.org/doi/10.1021/acs.energyfuels.5c05337.

Structural parameters of Cu, Zn, CuO, and CuO_2 estimating the range of chemical potentials for Cu in ZnO; details on the considered defect charge states and multiplicity for each defect; and additional electron and spin densities for selected defects (PDF)

■ AUTHOR INFORMATION

Corresponding Author

Francesco Ambrosio − *Dipartimento di Scienze di Base e Applicate (DISBA), Università degli Studi della Basilicata, 85100 Potenza, Italy;* orcid.org/0000-0002-6388-9586; Email: francesco.ambrosio@unibas.it

Author

Michele Loriso − *Dipartimento di Scienze di Base e Applicate (DISBA), Università degli Studi della Basilicata, 85100 Potenza, Italy*

Complete contact information is available at: https://pubs.acs.org/10.1021/acs.energyfuels.5c05337

Notes

The authors declare no competing financial interest.

■ ACKNOWLEDGMENTS

F.A. and M.L. thankfully acknowledge PRIN 2022-PNRR grant (P2022W9773) for funding. The authors also acknowledge the CINECA award under the ISCRA initiative, for the availability of high-performance computing resources: projects MHP-DEF (HP10CNQAEA), Photofix (HP10C2S6ML) and PAWS-ZnX (HP10CTDQYG).

■ REFERENCES

(1) Özgür, Ü.; Alivov, Y. I.; Liu, C.; Teke, A.; Reshchikov, M. A.; Doğan, S.; Avrutin, V.; Cho, S.-J.; Morkoç, H. A Comprehensive Review of ZnO Materials and Devices. *J. Appl. Phys.* **2005**, *98*, No. 041301.

(2) Klingshirn, C. ZnO: Material, Physics and Applications. *ChemPhysChem* **2007**, *8*, 782−803.

(3) Sharma, D. K.; Shukla, S.; Sharma, K. K.; Kumar, V. A Review on ZnO: Fundamental Properties and Applications. *Materials Today: Proceedings* **2022**, *49*, 3028−3035.

(4) Pearton, S.; Ren, F. Advances in ZnO-based Materials for Light Emitting Diodes. *Curr. Opin. Chem. Eng.* **2014**, *3*, 51−55.

(5) Rahman, F. Zinc oxide light-emitting diodes: a review. *Opt. Eng.* **2019**, *58*, No. 010901.

(6) Huang, J.; Yin, Z.; Zheng, Q. Applications of ZnO in Organic and Hybrid Solar Cells. *Energy Environ. Sci.* **2011**, *4*, 3861−3877.

(7) Savva, A.; Burgués-Ceballos, I.; Choulis, S. A. Improved Performance and Reliability of p-i-n Perovskite Solar Cells via Doped Metal Oxides. *Adv. Energy Mater.* **2016**, *6*, No. 1600285.

(8) Wang, D.; Wu, C.; Luo, W.; Guo, X.; Qu, B.; Xiao, L.; Chen, Z. ZnO/SnO_2 Double Electron Transport Layer Guides Improved Open Circuit Voltage for Highly Efficient $CH_3NH_3PbI_3$-Based Planar Perovskite Solar Cells. *ACS Appl. Energy Mater.* **2018**, *1*, 2215−2221.

(9) Zhong, S.; Morales-Masis, M.; Mews, M.; Korte, L.; Jeangros, Q.; Wu, W.; Boccard, M.; Ballif, C. Exploring Co-sputtering of ZnO: Al and SiO_2 for Efficient Electron-selective Contacts on Silicon Solar Cells. *Sol. Energy Mater. Sol. Cells* **2019**, *194*, 67−73.

(10) Mujtaba, A.; Khan, M.; Amami, M.; Alshahrani, D. O. Enhancing Perovskite Solar Cell Efficiency: ZnO-WO_3 as an Electron Transport Layer to Minimize Recombination Losses. *RSC Adv.* **2025**, *15*, 25019−25029.

(11) Krishna, K. G.; Umadevi, G.; Parne, S.; Pothukanuri, N. Zinc Oxide Based Gas Sensors and Their Derivatives: A Critical Review. *Journal of Materials Chemistry C* **2023**, *11*, 3906−3925.

(12) Franco, M. A.; Conti, P. P.; Andre, R. S.; Correa, D. S. A Review on Chemiresistive ZnO Gas Sensors. *Sens Actuators Rep.* **2022**, *4*, No. 100100.

(13) Zhu, L.; Zeng, W. Room-temperature gas sensing of ZnO-based gas sensor: A review. *Sensors and Actuators A: Physical* **2017**, *267*, 242−261.

(14) Labeau, M.; Rey, P.; Deschanvres, J.; Joubert, J.; Delabouglise, G. Thin films of High-resistivity Zinc Oxide Produced by a Modified CVD Method. *Thin Solid Films* **1992**, *213*, 94−98.

(15) Bhadwal, N.; Ben Mrad, R.; Behdinan, K. Review of Zinc Oxide Piezoelectric Nanogenerators: Piezoelectric Properties. *Composite Structures and Power Output. Sensors* **2023**, *23*, 3859.

(16) Kryshtab, T.; Khomchenko, V.; Papusha, V.; Mazin, M.; Tzyrkunov, Y. A. Thin ZnS: Cu, Ga and ZnO: Cu, Ga Film Phosphors. *Thin Solid Films* **2002**, *403*, 76−80.

(17) Abou Zeid, S.; Leprince-Wang, Y. Advancements in ZnO-based photocatalysts for Water Treatment: A Comprehensive Review. *Crystals* **2024**, *14*, 611.

(18) Di Mauro, A.; Fragalà, M. E.; Privitera, V.; Impellizzeri, G. ZnO for Application in Photocatalysis: From Thin Films to Nanostructures. *Mater. Sci. Semicond. Process.* **2017**, *69*, 44−51.

(19) Guo, Z.; Ambrosio, F.; Chen, W.; Gono, P.; Pasquarello, A. Alignment of Redox Levels at Semiconductor−Water Interfaces. *Chem. Mater.* **2018**, *30*, 94−111.

(20) Guo, Z.; Ambrosio, F.; Pasquarello, A. Evaluation of Photocatalysts for Water Splitting through Combined Analysis of Surface Coverage and Energy-Level Alignment. *ACS Catal.* **2020**, *10*, 13186−13195.

(21) Reynolds, D.; Look, D. C.; Jogai, B.; Litton, C.; Cantwell, G.; Harsch, W. Valence-band Ordering in ZnO. *Phys. Rev. B* **1999**, *60*, 2340.
(22) Madelung, O. *Semiconductors: Data Handbook*; Springer Science & Business Media: 2004.
(23) Janotti, A.; Van de Walle, C. G. Fundamentals of Zinc Oxide as a Semiconductor. *Rep. Prog. Phys.* **2009**, *72*, 126501.
(24) McCluskey, M. D.; Jokela, S. Defects in ZnO. *J. Appl. Phys.* **2009**, *106*, No. 071101.
(25) Muller, G. Optical and Electrical Spectroscopy of Zinc Oxide Crystals Simultaneously Doped with Copper and Donors. *Phys. Status Solidi B* **1976**, *76*, 525−532.
(26) Bharat, T.; Mondal, S.; Gupta, H.; Singh, P.; Das, A.; et al. Synthesis of Doped Zinc Oxide Nanoparticles: A Review. *Mater. Today Proc.* **2019**, *11*, 767−775.
(27) Samriti; Upadhyay, A.; Gupta, R.; Ruzimuradov, O.; Prakash, J.Recent Progress on Doped ZnO Nanostructures and its Photocatalytic Applications. In *Handbook of Green and Sustainable Nanotechnology: Fundamentals, Developments and Applications*; Springer: 2023; pp 1−30.
(28) Dietz, R.; Kamimura, H.; Sturge, M.; Yariv, A. Electronic Structure of Copper Impurities in ZnO. *Phys. Rev.* **1963**, *132*, 1559.
(29) Dingle, R. Luminescent Transitions Associated with Divalent Copper Impurities and the Green Emission from Semiconducting Zinc Oxide. *Phys. Rev. Lett.* **1969**, *23*, 579.
(30) Yan, Y.; Al-Jassim, M.; Wei, S.-H. Doping of ZnO by Group-IB Elements. *Appl. Phys. Lett.* **2006**, *89*, 181912.
(31) Lany, S.; Zunger, A. Polaronic Hole Localization and Multiple Hole Binding of Acceptors in Oxide Wide-gap Semiconductors. *Phys. Rev. B* **2009**, *80*, No. 085202.
(32) Lyons, J.; Alkauskas, A.; Janotti, A.; Van de Walle, C. Deep Donor State of the Copper Acceptor as a Source of Green Luminescence in ZnO. *Appl. Phys. Lett.* **2017**, *111*, No. 042101.
(33) Volnianska, O.; Bogusławski, P. Green Luminescence and Calculated Optical Properties of Cu Ions in ZnO. *J. Alloys Compd.* **2019**, *782*, 1024−1030.
(34) Pantelides, S. T. *Deep Centers in Semiconductors*; CRC Press: 1992.
(35) Gallino, F.; Di Valentin, C. Copper Impurities in Bulk ZnO: A Hybrid Density Functional Study. *J. Chem. Phys.* **2011**, *134*, 144506.
(36) Yang, Y.; Zhang, P.; Yang, J.; Wei, S.-H. Chemical Trend of a Cu Impurity in Zn Chalcogenides. *Phys. Rev. B* **2020**, *101*, No. 174101.
(37) Hou, Q.; Buckeridge, J.; Walsh, A.; Xie, Z.; Lu, Y.; Keal, T. W.; Guan, J.; Woodley, S. M.; Catlow, C. R. A.; Sokol, A. A. The Interplay of Interstitial and Substitutional Copper in Zinc Oxide. *Front. Chem.* **2021**, *9*, No. 780935.
(38) Reshchikov, M. A.; Avrutin, V.; Izyumskaya, N.; Shimada, R.; Morkoç, H.; Novak, S. About the Cu-related Green Luminescence Band in ZnO. *J. Vac. Sci. Technol. B:Nanotechnol.* **2009**, *27*, 1749−1754.
(39) McCluskey, M. D.; Corolewski, C. D.; Lv, J.; Tarun, M. C.; Teklemichael, S. T.; Walter, E. D.; Norton, M. G.; Harrison, K. W.; Ha, S. Acceptors in ZnO. *J. Appl. Phys.* **2015**, *117*, 112802.
(40) Yang, R.; Wang, F.; Lu, J.; Lu, Y.; Lu, B.; Li, S.; Ye, Z. ZnO with p-type Doping: Recent Approaches and Applications. *ACS Appl. Electron. Mater.* **2023**, *5*, 4014−4034.
(41) Garces, N.; Wang, L.; Bai, L.; Giles, N.; Halliburton, L.; Cantwell, G. Role of Copper in the Green Luminescence from ZnO Crystals. *Appl. Phys. Lett.* **2002**, *81*, 622−624.
(42) Reynolds, D.; Look, D. C.; Jogai, B. Fine Structure on the Green Band in ZnO. *J. Appl. Phys.* **2001**, *89*, 6189−6191.
(43) Ye, H.; Su, Z.; Tang, F.; Wang, M.; Chen, G.; Wang, J.; Xu, S. Excitation Dependent Phosphorous Property and New Model of the Structured Green Luminescence in ZnO. *Sci. Rep.* **2017**, *7*, 41460.
(44) Kanai, Y. K. Y. Admittance Spectroscopy of Cu-doped ZnO crystals. *Jpn. J. Appl. Phys.* **1991**, *30*, 703.
(45) Tynell, T.; Karppinen, M. Atomic Layer Deposition of ZnO: A Review. *Semicond. Sci. Technol.* **2014**, *29*, No. 043001.
(46) Gao, Z.; Banerjee, P. Atomic Layer Deposition of Doped ZnO Films. *J. Vac. Sci. Technol. A* **2019**, *37*, No. 050802.
(47) Del Sole, R.; Milella, A.; Fracassi, F.; Parlanti, P.; Gemmi, M.; Coclite, A. M.; Nocito, F.; Dibenedetto, A.; Palumbo, F. Comparison Between Thermal and Plasma-enhanced Atomic Layer Deposition of ZnO on Fullerene powder for Photocatalytic Dye Removal. *Mater. Res. Bull.* **2026**, *193*, No. 113659.
(48) Mohan, R.; Krishnamoorthy, K.; Kim, S.-J. Enhanced Photocatalytic Activity of Cu-doped ZnO Nanorods. *Solid State Commun.* **2012**, *152*, 375−380.
(49) Li, M.; Tu, X.; Wang, Y.; Su, Y.; Hu, J.; Cai, B.; Lu, J.; Yang, Z.; Zhang, Y. Highly Enhanced Visible-light-driven Photoelectrochemical Performance of ZnO-modified In_2S_3 Nanosheet Arrays by Atomic Layer Deposition. *Nano-Micro Lett.* **2018**, *10*, 45.
(50) Tian, Q.; Wu, W.; Yang, S.; Liu, J.; Yao, W.; Ren, F.; Jiang, C. Zinc Oxide Coating Effect for the Dye Removal and Photocatalytic Mechanisms of Flower-like MoS_2 Nanoparticles. *Nanoscale Res. Lett.* **2017**, *12*, 221.
(51) Wang, Y.; Ping, H.; Tan, T.; Wang, W.; Ma, P.; Xie, H. Enhanced Hydrogen Evolution from Water Splitting Based on ZnO Nanosheet/CdS Nanoparticle Heterostructures. *RSC Adv.* **2019**, *9*, 28165−28170.
(52) Al-Shami, A.; Sibari, A.; Mansouri, Z.; El Kassaoui, M.; El Kenz, A.; Benyoussef, A.; Loulidi, M.; Jouiad, M.; El Moutaouakil, A.; Mounkachi, O. Photocatalytic Properties of ZnO: Al/$MAPbI_3$/Fe_2O_3 Heterostructure: First-Principles Calculations. *International journal of molecular sciences* **2023**, *24*, 4856.
(53) Vaiano, V.; Iervolino, G. Photocatalytic Hydrogen Production from Glycerol Aqueous Solution Using Cu-Doped ZnO under Visible Light Irradiation. *Appl. Sci.* **2019**, *9*, 2741.
(54) Karthik, T.; Maldonado, A.; Olvera, M. D. l. L.; Hernández, A.; Vega-Pérez, J.; Gómez-Pozos, H. Copper-doped ZnO Thin Films Deposited by Spray Pyrolysis: Effect of Water Content in Starting Solution on Methylene Blue Degradation by Photocatalysis. *J. Electron. Mater.* **2021**, *50*, 5542−5552.
(55) Javed, M.; Qamar, M. A.; Shahid, S.; Alsaab, H. O.; Asif, S. Highly Efficient Visible Light Active Cu−ZnO/SgC_3N_4 Nanocomposites for Efficient Photocatalytic Degradation of Organic Pollutants. *RSC Adv.* **2021**, *11*, 37254−37267.
(56) Manzoor, M. F.; Ahmed, E.; Ahmad, M.; Ahmad, I.; Rana, A. M.; Ali, A.; Ghouri, M. I.; Manzoor, M. S.; Aziz, M. T. Enhanced Photocatalytic Activity of Hydrogen Evolution through Cu Incorporated ZnO Nano Composites. *Mater. Sci. Semicond. Process.* **2020**, *120*, No. 105278.
(57) Khumphon, J.; Ahmed, R.; Imboon, T.; Giri, J.; Chattham, N.; Mohammad, F.; Kityakarn, S.; Mangala Gowri, V.; Thongmee, S. Boosting Photocatalytic Activity in Rhodamine B Degradation Using Cu-Doped ZnO Nanoflakes. *ACS Omega* **2025**, *10*, 9337−9350.
(58) Butola, D.; Purohit, L. Exceptional stability and reusability of Cu-doped ZnO:SnO2 nanocomposites for photocatalysis under visible light. *Mater. Chem. Phys.* **2024**, *328*, No. 130021.
(59) Alatawi, N.; Saad, L. B.; Soltane, L.; Moulahi, A.; Mjejri, I.; Sediri, F. Enhanced solar photocatalytic performance of Cu-doped nanosized ZnO. *Polyhedron* **2021**, *197*, No. 115022.
(60) Wu, L.; Zhu, Y.; Liu, Y.; Yang, L.; Xu, L.; Mai, L. Cu-doped ZnO nanoarray trap enabling uniform Zn deposition for high-performance Zn-ion batteries. *Transactions of Materials Research* **2025**, *1*, No. 100097.
(61) Wahl, U.; Rita, E.; Correia, J.; Alves, E.; Soares, J. Lattice Location and Stability of Implanted Cu in ZnO. *Phys. Rev. B* **2004**, *69*, No. 012102.
(62) Warschkow, O.; Chuasiripattana, K.; Lyle, M.; Delley, B.; Stampfl, C. Cu/ZnO (0001) under Oxidating and Reducing Conditions: A First-principles Survey of Surface Structures. *Phys. Rev. B* **2011**, *84*, No. 125311.
(63) Cheng, Y.-T.; Liang, T.; Nie, X.; Choudhary, K.; Phillpot, S. R.; Asthagiri, A.; Sinnott, S. B. Cu Cluster Deposition on ZnO $10\bar{1}0$: Morphology and Growth mode Predicted from Molecular Dynamics Simulations. *Surf. Sci.* **2014**, *621*, 109−116.

https://doi.org/10.1021/acs.energyfuels.5c05337
Energy Fuels 2026, 40, 3397−3407

(64) Xi, C.; Nie, Y.; Wang, H.; Dong, C.; Han, J.; Du, X.-W. Thermal Methanol Synthesis from CO_2 Using Cu/ZnO Catalysts: Insights from First-Principles Calculations. *Small Struct.* **2025**, *6*, No. 2400345.
(65) Freysoldt, C.; Neugebauer, J.; Van de Walle, C. G. Fully *Ab Initio* Finite-Size Corrections for Charged-Defect Supercell Calculations. *Phys. Rev. Lett.* **2009**, *102*, No. 016402.
(66) Komsa, H.-P.; Rantala, T. T.; Pasquarello, A. Finite-Size Supercell Correction Schemes for Charged Defect Calculations. *Phys. Rev. B* **2012**, *86*, No. 045112.
(67) Ambrosio, F.; Miceli, G.; Pasquarello, A. Redox Levels in Aqueous Solution: Effect of van der Waals Interactions and Hybrid Functionals. *J. Chem. Phys.* **2015**, *143*, 244508.
(68) Ambrosio, F.; Wiktor, J.; Pasquarello, A. pH-Dependent Surface Chemistry from First Principles: Application to the $BiVO_4(010)$−Water Interface. *ACS Appl. Mater. Interfaces.* **2018**, *10*, 10011−10021.
(69) Di Liberto, G.; Maleki, F.; Pacchioni, G. pH Dependence of MgO, TiO_2, and γ-Al_2O_3 Surface Chemistry from First Principles. *J. Phys. Chem. C* **2022**, *126*, 10216−10223.
(70) Ambrosio, F.; Chen, W.; Pasquarello, A. Electronic Energy Levels of Aqueous Hydroxyl Species. *Phys. Chem. Chem. Phys.* **2025**, *27*, 23079.
(71) Falletta, S.; Wiktor, J.; Pasquarello, A. Finite-size Corrections of Defect Energy Levels Involving Ionic Polarization. *Phys. Rev. B* **2020**, *102*, No. 041115.
(72) Vegesna, S. V.; Bhat, V. J.; Bürger, D.; Dellith, J.; Skorupa, I.; Schmidt, O. G.; Schmidt, H. Increased Static Dielectric Constant in ZnMnO and ZnCoO Thin Films with Bound Magnetic Polarons. *Sci. Rep.* **2020**, *10*, 6698.
(73) Ashkenov, N.; Mbenkum, B.; Bundesmann, C.; Riede, V.; Lorenz, M.; Spemann, D.; Kaidashev, E.; Kasic, A.; Schubert, M.; Grundmann, M.; et al. Infrared Dielectric Functions and Phonon Modes of High-quality ZnO Films. *J. Appl. Phys.* **2003**, *93*, 126−133.
(74) Ambrosio, F.; Landi, A.; Loriso, M.; Leo, A.; Peluso, A. External Reorganization Energy upon Charge Transfer Reactions in Mildly Polar Media: The Case of Naphthalene in Tetrahydrofuran. *J. Phys. Chem. Lett.* **2025**, *16*, 6734−6744.
(75) Komsa, H.-P.; Pasquarello, A. Finite-size Supercell Correction for Charged Defects at Surfaces and Interfaces. *Phys. Rev. Lett.* **2013**, *110*, No. 095505.
(76) VandeVondele, J.; Krack, M.; Mohamed, F.; Parrinello, M.; Chassaing, T.; Hutter, J. Quickstep: Fast and Accurate Density Functional Calculations Using a Mixed Gaussian and Plane Waves Approach. *Comput. Phys. Commun.* **2005**, *167*, 103−128.
(77) VandeVondele, J.; Hutter, J. Gaussian Basis Sets for Accurate Calculations on Molecular Systems in Gas and Condensed Phases. *J. Chem. Phys.* **2007**, *127*, 114105.
(78) Kühne, T. D.; Iannuzzi, M.; Del Ben, M.; Rybkin, V. V.; Seewald, P.; Stein, F.; Laino, T.; Khaliullin, R. Z.; Schütt, O.; Schiffmann, F.; et al. CP2K: An Electronic Structure and Molecular Dynamics Software Package-Quickstep: Efficient and Accurate Electronic Structure Calculations. *J. Chem. Phys.* **2020**, *152*, 194103.
(79) Hartwigsen, C.; Gœdecker, S.; Hutter, J. Relativistic Separable Dual-Space Gaussian Pseudopotentials from H to Rn. *Phys. Rev. B* **1998**, *58*, 3641.
(80) Guidon, M.; Schiffmann, F.; Hutter, J.; VandeVondele, J. Ab Initio Molecular Dynamics Using Hybrid Density Functionals. *J. Chem. Phys.* **2008**, *128*, 214104.
(81) Guidon, M.; Hutter, J.; VandeVondele, J. Robust Periodic Hartree- Fock Exchange for Large-Scale Simulations Using Gaussian Basis Sets. *J. Chem. Theory Comput.* **2009**, *5*, 3010−3021.
(82) Guidon, M.; Hutter, J.; VandeVondele, J. Auxiliary Density Matrix Methods for Hartree-Fock Exchange Calculations. *J. Chem. Theory Comput.* **2010**, *6*, 2348−2364.
(83) Perdew, J. P.; Zunger, A. Self-Interaction Correction to Density-Functional Approximations for Many-Electron Systems. *Phys. Rev. B* **1981**, *23*, 5048−5079.
(84) Zhang, Y.; Yang, W. A Challenge for Density Functionals: Self-interaction Error Increases for Systems with a Noninteger Number of Electrons. *J. Chem. Phys.* **1998**, *109*, 2604−2608.
(85) Perdew, J. P.; Ernzerhof, M.; Burke, K. Rationale for Mixing Exact Exchange with Density Functional Approximations. *J. Chem. Phys.* **1996**, *105*, 9982−9985.
(86) Adamo, C.; Barone, V. Toward reliable density functional methods without adjustable parameters: The PBE0 model. *J. Chem. Phys.* **1999**, *110*, 6158−6170.
(87) Miceli, G.; Chen, W.; Reshetnyak, I.; Pasquarello, A. Nonempirical Hybrid Functionals for Band Gaps and Polaronic Distortions in Solids. *Phys. Rev. B* **2018**, *97*, No. 121112.
(88) Yang, J.; Falletta, S.; Pasquarello, A. Range-separated Hybrid Functionals for Accurate Prediction of Band Gaps of Extended Systems. *npj Comput. Mater.* **2023**, *9*, 108.
(89) Alkauskas, A.; Broqvist, P.; Pasquarello, A. Defect Energy Levels in Density Functional Calculations: Alignment and Band Gap Problem. *Phys. Rev. Lett.* **2008**, *101*, No. 046405.
(90) Alkauskas, A.; Broqvist, P.; Pasquarello, A. Defect Levels through Hybrid Density Functionals: Insights and Applications. *Phys. Status Solidi B* **2011**, *248*, 775−789.
(91) Heinemann, M.; Eifert, B.; Heiliger, C. Band Structure and Phase Stability of the Copper Oxides Cu_2O, CuO, and Cu_4O_3. *Phys. Rev. B* **2013**, *87*, No. 115111.
(92) Swank, R. K. Surface Properties of II-VI Compounds. *Phys. Rev.* **1967**, *153*, 844.
(93) Gouveia, A. F.; Lemos, S. C.; Leite, E. R.; Longo, E.; Andrés, J. Back to the Basics: Probing the Role of Surfaces in the Experimentally Observed Morphological Evolution of ZnO. *Nanomaterials* **2023**, *13*, 978.
(94) DiMucci, I. M.; Lukens, J. T.; Chatterjee, S.; Carsch, K. M.; Titus, C. J.; Lee, S. J.; Nordlund, D.; Betley, T. A.; MacMillan, S. N.; Lancaster, K. M. The Myth of d8 Copper(III). *J. Am. Chem. Soc.* **2019**, *141*, 18508−18520.
(95) Ambrosio, F.; Guo, Z.; Pasquarello, A. Absolute Energy Levels of Liquid Water. *J. Phys. Chem. Lett.* **2018**, *9*, 3212−3216.
(96) Trasatti, S. The Absolute Electrode Potential: An Explanatory Note (Recommendations 1986). *Pure Appl. Chem.* **1986**, *58*, 955−966.
(97) Ricciarelli, D.; Mosconi, E.; Wiktor, J.; Malavasi, L.; Ambrosio, F.; De Angelis, F. Electron Bipolarons at the $DMASnBr_3$−Water Interface: Effect on the Photocatalytic Hydrogen Production. *Int. J. Hydrogen Energy* **2024**, *58*, 863−871.
(98) Gono, P.; Wiktor, J.; Ambrosio, F.; Pasquarello, A. Surface Polarons Reducing Overpotentials in the Oxygen Evolution Reaction. *ACS Catal.* **2018**, *8*, 5847−5851.
(99) Ambrosio, F.; Wiktor, J. Charge Localization in Optoelectronic and Photocatalytic Applications: Computational perspective. *Appl. Phys. Lett.* **2025**, *126*, 130501.

https://doi.org/10.1021/acs.energyfuels.5c05337
Energy Fuels 2026, 40, 3397−3407